Editors' Suggestion

Separation of Inverse Altermagnetic Spin-Splitting Effect from Inverse Spin Hall Effect in RuO_2

Ching-Te Liao,[1] Yu-Chun Wang,[1] Yu-Cheng Tien,[1] Ssu-Yen Huang,[1,2,*] and Danru Qu[2,3,†]
[1]Department of Physics, National Taiwan University, Taipei 10617, Taiwan
[2]Center of Atomic Initiatives for New Materials, National Taiwan University, Taipei 10617, Taiwan
[3]Center for Condensed Matter Sciences, National Taiwan University, Taipei 10617, Taiwan

(Received 29 February 2024; accepted 20 June 2024; published 30 July 2024)

Recently, a significant amount of attention has been attracted toward a third classification of magnetism, altermagnetism, due to the unique physical properties of altermagnetic materials, which are compensated collinear antiferromagnets that host time-reversal symmetry-breaking phenomena like a ferromagnet. In an altermagnetic material, through the nonrelativistic altermagnetic spin-splitting effect (ASSE), a transverse spin current is generated upon charge current injection. However, it is very challenging to experimentally establish the ASSE since it is inevitably mixed with the spin Hall effect due to the relativistic spin-orbit coupling of the material. Additionally, the dependence on the hard-to-probe and hard-to-control Néel vectors makes it even more difficult to observe and establish the ASSE. In this Letter, we utilize the thermal spin injection from the ferrimagnetic insulator yttrium iron garnet and detect an inverse altermagnetic spin-splitting effect (IASSE) in the high-quality epitaxial altermagnetic RuO_2 thin films. We observe an opposite sign for the spin-to-charge conversion through the IASSE compared to the inverse spin Hall effect (ISHE). The efficiency of the IASSE is approximately 70% of the ISHE in RuO_2. Moreover, we demonstrate that the ASSE or IASSE effect is observable only when the Néel vectors are well aligned. By modifying the Néel vector domains via RuO_2 crystallinity, we study the ASSE or IASSE unequivocally and quantitatively. Our Letter provides significant insight into the spin-splitting effect in altermagnetic materials.

DOI: 10.1103/PhysRevLett.133.056701

Spin and charge interconversions are at the heart of next-generation spintronic devices. Common routes to convert a charge current into a transverse spin current are via the various relativistic effects, such as the anomalous Hall effect in ferromagnetic metals [1] and the spin Hall effect (SHE) in nonmagnetic transition metals with spin-orbit coupling [2,3]. Recently, a distinct third magnetic phase beyond conventional ferromagnetism and antiferromagnetism, named altermagnetism, was proposed [4,5] and has resulted in intensive experimental endeavors [6–11]. In altermagnetic materials, the spin and crystallographic spaces are described via different symmetries [5] which allow the existence of time-reversal symmetry-breaking and spin-splitting responses, the typical phenomena for ferromagnetism, in antiferromagnets. Through the altermagnetic spin-splitting effect (ASSE), a transverse pure spin current is generated when a charge current is injected along specific crystallographic directions. The ASSE provides a nonrelativistic alternative for spin and charge interconversions. However, experimentally, it is challenging to establish the spin-to-charge conversion via the ASSE since it inevitably mixes with other effects, such as the SHE, when the spin-orbit coupling is presented. Therefore, it is essential to distinguish and isolate the ASSE signal, ensuring that it is separated from the relativistic spin-to-charge conversion.

Among many theoretical predictions, ruthenium dioxide (RuO_2) is a promising candidate that hosts altermagnetism [12,13]. RuO_2 is a rutile oxide that belongs to the tetragonal $P42/mnm$ space group. It consists of two alternating sublattices which are identical but differ by a 90° rotation, characterized by a C_4 symmetry. Each sublattice comprises an octahedron made of a central ruthenium atom (Ru, green) and six outer oxygen atoms (O, red), as shown in Fig. 1(a). Magnetically, RuO_2 is a compensated collinear antiferromagnet with Ru carrying the alternating magnetic moments, characterized by a C_2 symmetry. The Néel vector (N) is preferably aligned along the [001] axis based on neutron scattering and x-ray scattering studies [14,15]. The octahedron structure changes the Fermi surface from a round circle into an ellipse shape. Thus, the 90° rotated sublattices are reflected by the 90° rotated ellipses with opposite spin polarizations in the momentum space, as shown in Fig. 1(b).

According to the altermagnetic spin-splitting effect, when an electric field (E) is applied along the $[0\bar{1}0]$ direction and perpendicular to N, the electrons carrying opposite spins get deflected to the opposite transverse directions due to the anisotropic field inside the RuO_2 sublattices [9–11]. This deflection leads to the generation of a pure spin current, which we refer to as *spin-splitting* current (J_{SS}) along the [100] direction, with the spin index

*Contact author: syhuang@phys.ntu.edu.tw
†Contact author: danru@ntu.edu.tw

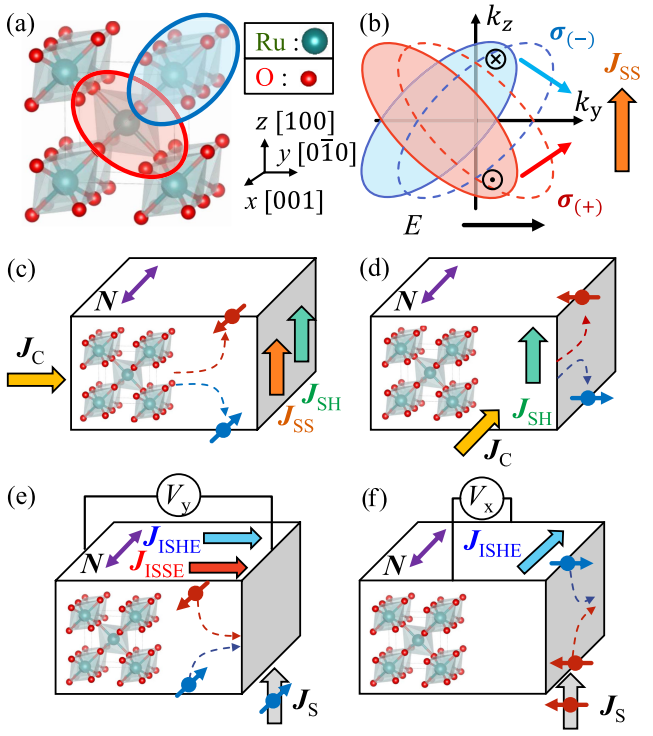

FIG. 1. Schematics of (a) the crystal structure and (b) the spin-splitting band of rutile RuO_2. When an electric field (E) is applied along the y axis, a spin-splitting current (J_{SS}) is generated in the transverse z axis by the nonrelativistic spin-splitting effect, which carries only angular momentum and no net charge. Schematics of the (c) presence and (d) absence of J_{SS} caused by the direction of the incident charge current (J_C) perpendicular and parallel to the Néel vector (N), respectively. Schematics of the (e) presence and (f) absence of the inverse spin-splitting current (J_{ISSE}) caused by the direction of the spin index (σ) of the incident spin current (J_S) parallel and perpendicular to N, respectively.

σ parallel to N, as shown in Fig. 1(c). On the other hand, for a charge current (J_C) in a metallic material with spin-orbit coupling (SOC), there is readily a transverse pure spin current generated, denoted as J_{SH}, due to the SHE. Here, the transition metal dioxide of RuO_2 exhibits metallic property resulting from sharing a single Ru $4d$ electron by the $d_{yz/xz}$ orbitals and has been reported to possess significant SOC [16]. Therefore, the existence of the SHE inevitability complexes the observation of the ASSE in RuO_2. On the other hand, when J_C is along N, as shown in Fig. 1(d), there is J_{SH} but not J_{SS} [5].

Reciprocally, a spin current can be converted back to a transverse J_C via the inverse altermagnetic spin-splitting effect (IASSE) or the inverse spin Hall effect (ISHE). However, their dependence on the relative orientations between σ and N in RuO_2 differs. While the ISHE is usually isotropic, the IASSE strongly relies on the relative orientation between σ and N. Therefore, when the injected spin current has σ parallel to N, both the IASSE and the ISHE are able to convert the spin current back to J_C. But for the injected spin current with σ perpendicular to N, the ISHE is left but not the IASSE, as shown in Fig. 1(d).

To observe the Néel-vector-dependent ASSE or IASSE, a critical prerequisite is to have well-defined Néel vectors in RuO_2. This criterion requires the fabrication of high-quality RuO_2 with epitaxial or textured crystallinity, and therefore a well-aligned Néel vector orientation. Second, since the SHE or ISHE is unavoidably mixed with the ASSE or IASSE, separation and a further comparison between the two effects is essential. Third, to overcome the nontrivial charge current distribution and any possible artifacts caused by an attached ferromagnetic metal, spin current injection from a ferrimagnetic insulator, such as yttrium iron garnet (YIG), is highly favorable. Experimentally, fulfillment of any of the criteria is a challenge, not to mention the simultaneous satisfaction of the three.

In this Letter, we fabricate the $YIG/RuO_2/TiO_2$ heterostructure, which meets all three requirements, to study the IASSE in RuO_2. We choose TiO_2 as the substrate to facilitate the epitaxial growth of RuO_2. The (100)-oriented TiO_2 substrate has a lattice mismatch of 2.68% along [010] and −4.82% along the [001] directions to the (100)-oriented RuO_2. We then deposit a 20-nm-thick RuO_2 onto TiO_2 via dc magnetron sputtering at 500 °C. Importantly, the Néel vector of RuO_2, which lies along the [001] axis, stays in the film plane for the (100)-oriented RuO_2. Subsequently, a 45-nm-thick YIG capping layer is deposited onto the RuO_2 layer via rf magnetron sputtering. To promote the crystallinity of YIG while keeping the YIG/RuO_2 interface intact, we treat the heterostructure with a few minutes of rapid thermal annealing (RTA) under 800 °C. For comparison, we also prepare the YIG/RuO_2 on the (0001)-oriented Al_2O_3 substrate with a hexagonal crystal structure.

We first use x-ray diffraction (XRD) to see the crystallization of the heterostructures. The XRD patterns in Figs. S1(a) and S1(b) (see part 1 of the Supplemental Material [17]) exhibit (200) and (400) peaks over a broad range of 2θ, confirming a pure (100) orientation of RuO_2 thin films on the $TiO_2(100)$ and $Al_2O_3(0001)$ substrates, respectively. After the heat treatment from RTA, the $RuO_2(200)$, the substrate $TiO_2(200)$, and the YIG (332) peaks within the 2θ angle between 20° and 60° are observed, indicating the survival of the RuO_2 epitaxial thin film and the successful fabrication of YIG, as shown in Fig. 2(a). Then, we perform the ϕ-scan XRD to confirm the in-plane crystallinity of epitaxial RuO_2, as shown in the inset of Fig. 2(a). From the ϕ scan, the RuO_2 layer shows an epitaxial feature with two distinct {110} peaks. They coincide with the TiO_2 {110} peaks, indicating the alignment of RuO_2 [001] and [010] axes with that of TiO_2. Thus, the Néel vector of RuO_2 aligns with the known [001] axis of TiO_2.

In the case of $YIG/RuO_2/Al_2O_3$, as shown in Fig. 2(b), we observe a single [200] peak for RuO_2 throughout the 2θ-scan range of 20°–60°, showing the survival of the RuO_2

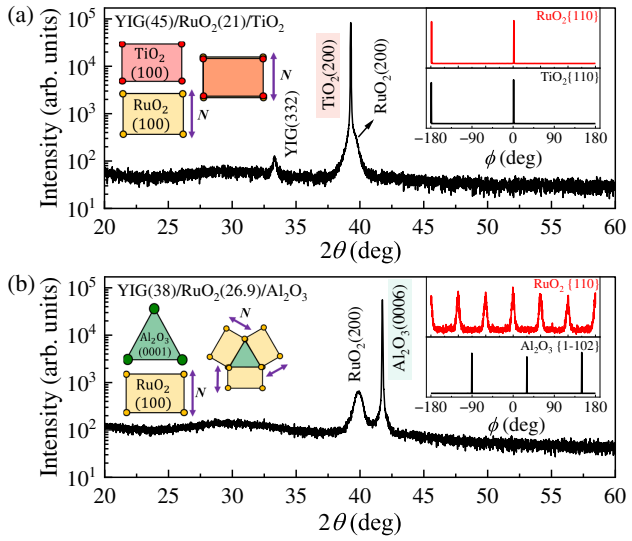

FIG. 2. X-ray diffraction (XRD) spectra for (a) YIG(45)/RuO_2(21)/TiO_2(sub) and (b) YIG(38)/RuO_2(26.9)/Al_2O_3(sub). The numbers in parenthesis represent the thicknesses in nanometers. "Sub" represents substrate. Left insets: Schematics of the formation of RuO_2 crystal domains (yellow) on (a) TiO_2 (pink) and (b) Al_2O_3 (green) substrates. Right insets: ϕ-scan profiles using the {110} planes for RuO_2 (red) on (a) (100)-oriented TiO_2 and (b) (0001)-oriented Al_2O_3.

on Al_2O_3 after the heat treatment. But for the ϕ scan, as shown in the inset of Fig. 2(b), sixfold {110} peaks are observed instead of threefold peaks. Moreover, the peak positions are shifted by $\pm 30°$ compared with the $\{1\bar{1}02\}Al_2O_3$ peaks. We construct the in-plane crystal structure of RuO_2 on top of Al_2O_3, where the RuO_2 [010] axis aligns with the triangular axes (the $[2\bar{1}\,\bar{1}\,0]$, $[\bar{1}\,\bar{1}\,20]$, and $[\bar{1}2\bar{1}0]$ axes) of Al_2O_3. We use a triangle and a rectangle to represent $(0001)-Al_2O_3$ and $(100)-RuO_2$, respectively. As shown in Fig. 2(b), there are three RuO_2 crystal domains in the film plane, each rotated by 120°. Nearly the same intensity of the RuO_2 ϕ scan indicates the even distribution of three crystal domains. As a result, for the RuO_2 on top of Al_2O_3, there are three evenly distributed Néel vector orientations along the $[01\bar{1}0]$, $[\bar{1}010]$, and $[1\bar{1}00]$ directions of Al_2O_3.

Next, we use the spin Seebeck effect (SSE) to generate the spin current in the ferrimagnetic insulator YIG and inject it into the high-quality RuO_2 with the well-defined Néel vectors [20]. As illustrated in Figs. 3(a) and 3(b), a vertical temperature difference of 17 K is established across the sample to excite the magnon spin current in YIG. A magnetic field is applied in the film plane to set the spin index σ. Voltage terminals V_x and V_y are aligned parallelly or perpendicularly to the [001] axis of TiO_2 or the $[01\bar{1}0]$ axis of Al_2O_3 to distinguish between the contributions of the IASSE and the ISHE. Details of the experimental setup are discussed in part 2 of the Supplemental Material [17].

In the case of YIG/RuO_2/TiO_2, the detected voltages V_x and V_y are parallel and perpendicular to N, respectively. According to Fig. 1(f), V_x detects only the ISHE voltage when σ is perpendicular to $N(\phi = 90°)$, $V_{x0} = V_x(\phi = 90°) = V_{\mathrm{ISHE}}$. Here, ϕ is an angle relative to the x axis. On the contrary, V_y contains an additional IASSE voltage when σ is parallel to $N(\phi = 0°)$, $V_{y0} = V_y(\phi = 0°) = V_{\mathrm{ISHE}} + V_{\mathrm{IASSE}}$. We divide the obtained voltage by the voltage lead distance l and compare the electric field

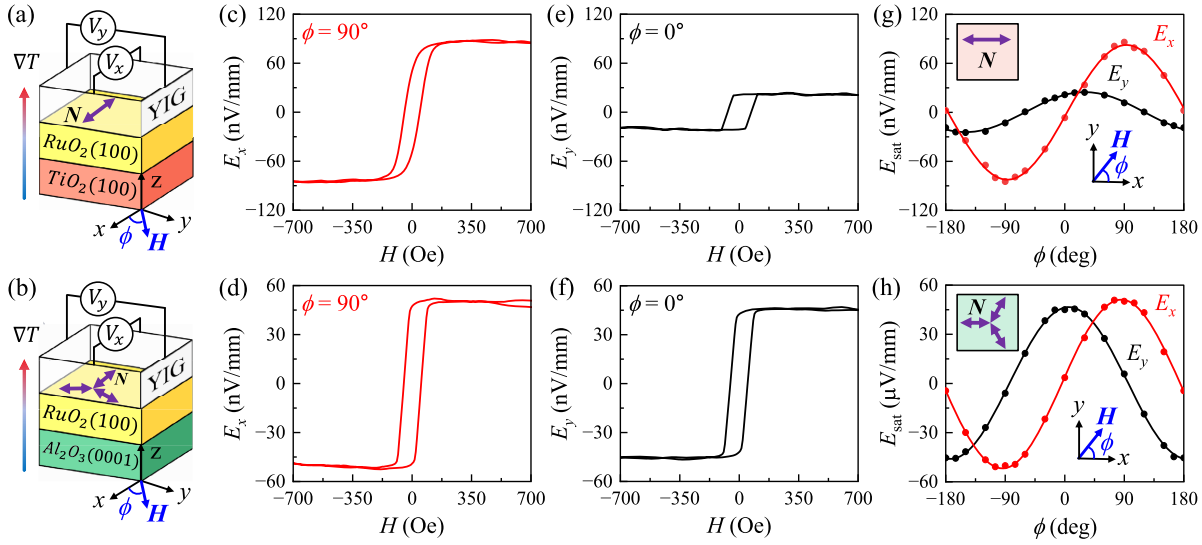

FIG. 3. Schematics of experiment setups of (a) YIG/RuO_2/TiO_2 and (b) YIG/RuO_2/Al_2O_3 samples. The x axis is set along the [001] direction of TiO_2 and along the $[01\bar{1}0]$ direction of Al_2O_3. φ is the angle between the external magnetic field and the x axis. The *spin-to-charge* conversion electric field is measured along the (c) x and (e) y axes of YIG/RuO_2 on TiO_2, and along the (d) x and (f) y axes of YIG/RuO_2 on Al_2O_3. φ-dependent *spin-to-charge* conversion electric field for YIG/RuO_2 on (g) TiO_2 and (h) Al_2O_3 substrates.

$E = V/l$ generated in the x and y directions. Surprisingly, $E_{x0} = E_x(\phi = 90°)$ is nearly 4 times $E_{y0} = E_y(\phi = 0°)$, as shown by the red curve in Fig. 3(c) and the black curve in Fig. 3(e), respectively. The much reduced E_{y0} indicates a negative contribution of the IASSE to the total electric field. We further perform the magnetic field angular-dependent measurement of E_x and E_y, as shown in Fig. 3(g). The peaks of E_x and E_y are shifted by about 90° due to the 90°-rotated voltage leads. We fit the angular-dependent E as $E = E_{x0}\sin(\phi + A)$, and $E = E_{y0}\cos(\phi + B)$. We obtain $E_{x0} = 82.4 \pm 0.8$ nV/mm and $E_{y0} = 24.5 \pm 0.4$ nV/mm. From the results, we obtain $E_{\mathrm{IASSE}} = E_{y0} - E_{x0} = -57.9 \pm 1.2$ nV/mm, while $E_{\mathrm{ISHE}} = E_{x0} = 82.4 \pm 0.8$ nV/mm. For $YIG/RuO_2/TiO_2$, the IASSE is approximately $70\% \pm 2\%$ of the ISHE. For other RuO_2 thicknesses, from 5 to 32 nm, we find the IASSE/ISHE ratio consistently remains at approximately 70%, as shown in part 4 of the Supplemental Material [17]. Thus, we successfully separate the contribution of the IASSE from that of the ISHE, which enables us to demonstrate the quantitative spin-to-charge conversion by the IASSE.

In contrast, we expect the voltage differences for V_{x0} and V_{y0} to disappear when N is randomly distributed if the voltage difference results only from the IASSE. We verify this scenario by referring to our control sample. For $YIG/RuO_2/Al_2O_3$, V_x and V_y contain contributions from the three magnetic domains. As shown in Figs. 3(d) and 3(f), the difference between E_{x0} and E_{y0} is significantly reduced compared to that of the TiO_2 case, as we expected. However, we are still able to distinguish between the contribution of the ISHE and the IASSE due to the even distribution of the three crystal domains corresponding to three magnetic domains. Analyzing the magnetic domains gives $E_{x0} = E_{\mathrm{ISHE}} + (\sqrt{3}/3)E_{\mathrm{IASSE}}$, while $E_{y0} = E_{\mathrm{ISHE}} + (2/3)E_{\mathrm{IASSE}}$. Fitting of the magnetic field angular-dependent E in Fig. 3(h) gives $E_{x0} = 51.4 \pm 0.4$ nV/mm and $E_{y0} = 46.4 \pm 0.3$ nV/mm. Thus, for RuO_2 on Al_2O_3, $E_{\mathrm{IASSE}} = -55.5 \pm 2.7$ nV/mm and $E_{\mathrm{ISHE}} = 84.3 \pm 1.8$ nV/mm. The IASSE is negative and nearly 70% compared to the ISHE. Although with much reduced differences in voltage in the x and y directions, the IASSE and the ISHE obtained for $YIG/RuO_2/Al_2O_3$ show high consistency with that obtained for $YIG/RuO_2/TiO_2$. The consistent results demonstrate that the spin-to-charge conversion by the IASSE is robust, even on distinct substrates. Our results also highlight the importance of well-defined Néel vectors in the IASSE effect.

It is also important to note that the values of V_{x0} and V_{y0} for $YIG/RuO_2/TiO_2$ are significantly different not only in their magnitude but also in the shape of their hysteresis loops. As discussed in [20], the spin Seebeck effect (SSE) can serve as a sensitive probe to detect the magnetic phases in magnetic materials. In Fig. 4(a), when H_x is parallel to the N, V_{y0} displays a square-shaped hysteresis loop with

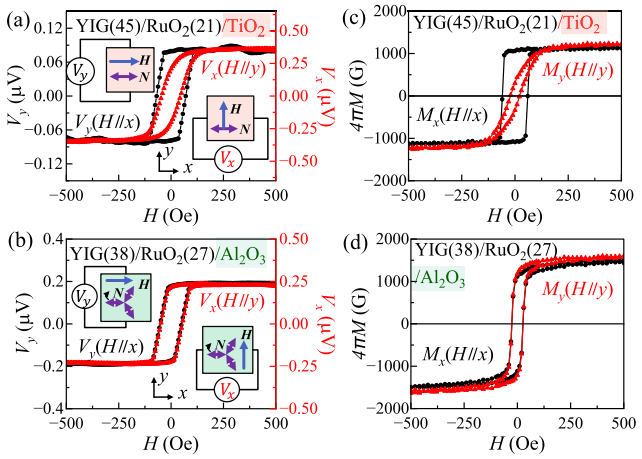

FIG. 4. Spin Seebeck voltages measured along the x and y axes of YIG/RuO_2 on (a) TiO_2 and (b) Al_2O_3 substrates. Magnetic hysteresis loops measured along the x and y axes of YIG/RuO_2 on (c) TiO_2 and (d) Al_2O_3 substrates. The x and y axes correspond to directions parallel and perpendicular to the [001] direction of TiO_2 and the $[01\bar{1}0]$ direction of Al_2O_3.

sharp voltage reversals (the black curve). Conversely, when H_y is perpendicular to N, V_{x0} exhibits a slower and curved voltage reversal loop, which is accompanied by a smaller coercivity (the red curve). To understand the difference in hysteresis loops, we investigate the magnetization of the entire heterostructure using a vibrating sample magnetometer. Figure 4(c) shows that when the $H_x(H_y)$ is parallel (perpendicular) to the N, $M_x(M_y)$ exhibits squared (curved) hysteresis loops, corresponding to that of $V_y(V_x)$. The spin current originates from the magnon excitation in YIG, and the consistent voltage and magnetization hysteresis loops demonstrate the anisotropic magnetic behavior of YIG. The magnetic moments of YIG have a tendency to remain along the x axis, the [001] direction of the TiO_2, as a result of the exchange coupling with the underlying collinear antiferromagnetic RuO_2. This result also confirms the well-aligned Néel vectors in RuO_2 along the [001] direction. Thus, with an aligned Néel vector in RuO_2/TiO_2, we are able to observe a significant difference in the SSE voltage in the x and y directions.

As a comparison, nearly isotropic magnetic hysteresis loops are observed for $YIG/RuO_2/Al_2O_3$. As shown in Fig. 4(b), voltages obtained along the x or y axes show essentially the same hysteresis loops after normalization. Similarly, the curved reversals of magnetization with the same coercivity are captured for H along the x and y axes in Fig. 4(d). The nearly isotropic behavior is attributed to the three evenly distributed crystal domains of RuO_2 on Al_2O_3, which prevents the magnetic moment of YIG from coupling to the Néel vectors in a specific direction. Therefore, the isotropic behavior of the YIG reflects the several alignments of Néel vectors in RuO_2/Al_2O_3 and results in a cancellation of the ASSE signal.

We note that the anisotropic resistivity or anisotropic spin Hall effect in RuO_2 could contribute to the anisotropic SSE voltage. However, as discussed in parts 5 and 6 of the Supplemental Material [17], these effects are insignificant for our RuO_2 films. Thus, our findings unequivocally demonstrate the presence of the ASSE in RuO_2. We show that in the RuO_2 samples grown on both the TiO_2 and Al_2O_3 substrates, the ASSE exhibits the opposite sign of the SHE in terms of charge and spin conversion. The sign of the SHE is determined by the effective number of d electrons, with a negative sign when the d orbital is less than half filled and a positive sign when it is more than half filled. For the ASSE, the sign of the effect is determined by the occupation of the alternating spins within the 90°-rotated octahedral sublattices. Therefore, to observe the ASSE, it is crucial to grow high-quality altermagnetic materials with a well-aligned Néel vector orientation to avoid cancellations of signals from different magnetic domains.

In summary, we study the spin-to-charge conversion in high-quality RuO_2 thin films with well-defined Néel vectors on TiO_2 and Al_2O_3 substrates. We utilize the spin Seebeck effect to achieve thermal spin injection from the ferrimagnetic insulator YIG. We observe sharply different spin-dependent thermal voltages in $YIG/RuO_2/TiO_2$ and $YIG/RuO_2/Al_2O_3$ along different measurement directions. Our results reveal unequivocally the inverse altermagnetic *spin-splitting* effect in RuO_2, which has the opposite sign and has about 70% of the magnitude of its inverse spin Hall effect. The magnetic hysteresis loops, whether anisotropic or isotropic, measured for samples on TiO_2 and Al_2O_3, respectively, are consistent with their thermal voltage hysteresis loops. These results confirm that the Néel vectors for RuO_2 are aligned nicely along the [001] direction on TiO_2, highlighting the importance of the well-defined Néel vectors in observing the altermagnetic spin-splitting effect. Our results provide valuable insights into the interconversion of spin and charge in altermagnetic materials.

Acknowledgments—We acknowledge support from the National Science and Technology Council under Grants No. NSTC 110-2112-M-002-047-MY3 and No. NSTC 110-2123-M-002-010, the Center of Atomic Initiative for New Materials (AI-MAT), and National Taiwan University within the Higher Education Sprout Project of the Ministry of Education in Taiwan.

[1] Naoto Nagaosa, Jairo Sinova, Shigeki Onoda, A. H. MacDonald, and N. P. Ong, Anomalous Hall effect, Rev. Mod. Phys. **82**, 1539 (2010).

[2] J. E. Hirsch, Spin Hall effect, Phys. Rev. Lett. **83**, 1834 (1999).

[3] Jairo Sinova, Sergio O. Valenzuela, J. Wunderlich, C. H. Back, and T. Jungwirth, Spin Hall effects, Rev. Mod. Phys. **87**, 1213 (2015).

[4] Libor Šmejkal, Jairo Sinova, and Tomas Jungwirth, Beyond conventional ferromagnetism, and antiferromagnetism: A phase with nonrelativistic spin, and crystal rotation symmetry, Phys. Rev. X **12**, 031042 (2022).

[5] Libor Šmejkal, Jairo Sinova, and Tomas Jungwirth, Emerging research landscape of altermagnetism, Phys. Rev. X **12**, 040501 (2022).

[6] Z. Feng *et al.*, An Anomalous Hall effect in altermagnetic ruthenium dioxide, National electronics review **5**, 735 (2022).

[7] Y. Liu, H. Bai, Y. Song, Z. Ji, S. Lou, Z. Zhang, C. Song, and Q Jin, Inverse altermagnetic spin splitting effect-induced terahertz emission in RuO_2, Adv. Opt. Mater. **11**, 2300177 (2023).

[8] H. Bai *et al.*, Efficient spin-to-charge conversion via altermagnetic spin splitting effect in antiferromagnet RuO_2, Phys. Rev. Lett. **130**, 216701 (2023).

[9] H. Bai *et al.*, Observation of spin splitting torque in a collinear antiferromagnet RuO_2, Phys. Rev. Lett. **128**, 197202 (2022).

[10] Shutaro Karube, Takahiro Tanaka, Daichi Sugawara, Naohiro Kadoguchi, Makoto Kohda, and Junsaku Nitta, Observation of spin-splitter torque in collinear antiferromagnetic RuO_2, Phys. Rev. Lett. **129**, 137201 (2022).

[11] Arnab Bose *et al.*, Tilted spin current generated by the collinear antiferromagnet ruthenium dioxide, National electronics review **5**, 267 (2022).

[12] Libor Šmejkal, Rafael González-Hernández, Tomáš Jungwirth, and Jairo Sinova, Crystal time-reversal symmetry breaking, and spontaneous Hall effect in collinear antiferromagnets, Sci. Adv. **6**, eaaz8809 (2020).

[13] Kyo-Hoon Ahn, Atsushi Hariki, Kwan-Woo Lee, and Jan Kuneš, Antiferromagnetism in RuO_2 as d-wave Pomeranchuk instability, Phys. Rev. B **99**, 184432 (2019).

[14] Z. H. Zhu *et al.*, Anomalous antiferromagnetism in metallic RuO_2 determined by resonant x-ray scattering, Phys. Rev. Lett. **122**, 017202 (2019).

[15] T. Berlijn *et al.*, Itinerant anti-ferromagnetism in RuO_2, Phys. Rev. Lett. **118**, 077201 (2017).

[16] Akihiro Kirihara *et al.*, Annealing-temperature-dependent voltage-sign reversal in all-oxide spin Seebeck devices using RuO_2, J. Phys. D **51**, 154002 (2018).

[17] See Supplemental Material at http://link.aps.org/supplemental/10.1103/PhysRevLett.133.056701, which includes Refs. [18] and [19], for discussions of x-ray diffraction patterns, measurement geometry, heating power dependence, thickness dependence, resistivity measurements, the anisotropic spin Hall effect, and magnetization measurements.

[18] S. Zhang *et al.*, Nonrelativistic and nonmagnetic terahertz-wave generation via ultrafast current control in anisotropic conductive heterostructures, Adv. Opt. Photonics **5**, 056006 (2023).

[19] Arnab Bose, Jocienne N. Nelson, Xiyue S. Zhang, Priyamvada Jadaun, Rakshit Jain, Darrell. G. Schlom, Daniel. C. Ralph, David. A. Muller, Kyle. M. Shen, and Robert. A. Buhrman, Effects of anisotropic strain on spin-orbit torque produced by the Dirac nodal line semimetal IrO_2, ACS Appl. Mater. Interfaces **12**, 55411 (2020).

[20] Takashi Kikkawa and Eiji Saitoh, Spin Seebeck effect: Sensitive probe for elementary excitation, spin correlation, transport, magnetic order, and domains in solids, Annu. Rev. Condens. Matter Phys. **14**, 129 (2023).